JACS Au
AN OPEN ACCESS JOURNAL OF THE AMERICAN CHEMICAL SOCIETY
pubs.acs.org/jacsau
Article

Electrochemical CO_2 Reduction Reaction over Cu Nanoparticles with Tunable Activity and Selectivity Mediated by Functional Groups in Polymeric Binder

Qiaowan Chang,[†] Ji Hoon Lee,[†] Yumeng Liu,[†] Zhenhua Xie, Sooyeon Hwang, Nebojsa S. Marinkovic, Ah-Hyung Alissa Park,* Shyam Kattel,* and Jingguang G. Chen*

Cite This: *JACS Au* 2022, 2, 214−222
Read Online

ABSTRACT: The electrochemical carbon dioxide reduction reaction (CO_2RR) using copper (Cu)-based catalysts has received significant attention mainly because Cu is an element capable of producing hydrocarbons and oxygenates. One possible way to control the CO_2RR performance at the electrode interface is by modifying catalysts with specific functional groups of different polymeric binders, which are necessary components in the process of electrode fabrication. However, the modification effect of the key functional groups on the CO_2RR activity and selectivity is poorly understood over Cu-based catalysts. In this work, the role of functional groups (*e.g.*, −COOH and $-CF_2$ groups) in hydrophilic and hydrophobic polymeric binders on the CO_2RR of Cu-based catalysts is investigated using a combination of electrochemical measurements, *in situ* characterization, and density functional theory (DFT) calculations. DFT results reveal that functional groups influence the binding energies of key intermediates involved in both CO_2RR and the competing hydrogen evolution reaction, consistent with experimental observation of binder-dependent product distributions among formic acid, CO, CH_4, and H_2. This study provides a fundamental understanding that the selection of desired polymeric binders is a useful strategy for tuning the CO_2RR activity and selectivity.

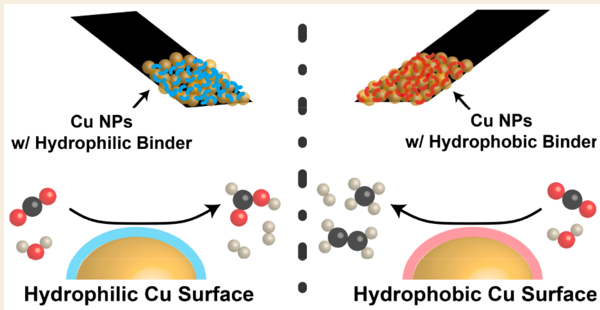

KEYWORDS: *polymeric binders, functional groups, copper, carbon dioxide reduction, density functional theory*

1. INTRODUCTION

The electrochemical CO_2 reduction reaction (CO_2RR)[1−7] has been the subject of many investigations in the past decades because this process can potentially provide an alternative way to upgrade CO_2 into value-added chemicals using electrons from renewable energy resources. Recent efforts[8−29] to search for different catalysts for CO_2RR have identified copper (Cu) as an element that can produce hydrocarbons and oxygenates, including methane (CH_4), ethylene (C_2H_4), carbon monoxide (CO), formic acid (HCOOH), methanol (CH_3OH), ethanol (C_2H_5OH), and acetone (C_3H_6O). The versatile CO_2RR properties of Cu primarily originate from the optimal *CO binding energy on Cu surfaces,[8,9] which allows the further hydrogenation of adsorbed *CO into hydrocarbon or oxygenate species without poisoning the catalyst surfaces and enables the C−C coupling between *CO and/or *CO/*CHO/*COH (* refers to adsorbed intermediates). However, due to the presence of multiple potential-dependent CO_2RR reaction pathways and the competitive hydrogen evolution reaction (HER), achieving high selectivity toward a single product on Cu catalysts remains a challenge.

Therefore, most recent studies on Cu-based CO_2RR electrocatalysts have been mainly focused on modulating product distribution. In an effort to modify the electronic state of Cu, controlling crystal facets[10,11] (*e.g.*, Cu(100) versus Cu(111)), enriching defective sites[12,13] (*e.g.*, point defect and grain boundary), adopting three-dimensional structures[14] (*e.g.*, inverse opals), isolating a Cu atom (Cu-single atom catalyst),[15,30,31] and alloying with other metallic components[16−21,32] have been investigated because these approaches can tune the binding energies of key reaction intermediates. In addition, the chemistry at the catalyst−electrolyte interface[22] has also been explored. This approach includes the addition of halide-containing salts[23] (*i.e.*, KI, KBr, and KCl, *etc.*) in an electrolyte and the use of various alkali ions[24,25,33] (*i.e.*, $AHCO_3$, A = Li^+, Na^+, K^+, and Cs^+), which lead to a different

Received: November 1, 2021
Published: December 9, 2021

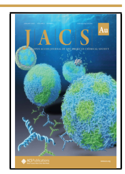

https://doi.org/10.1021/jacsau.1c00487
JACS Au 2022, 2, 214−222

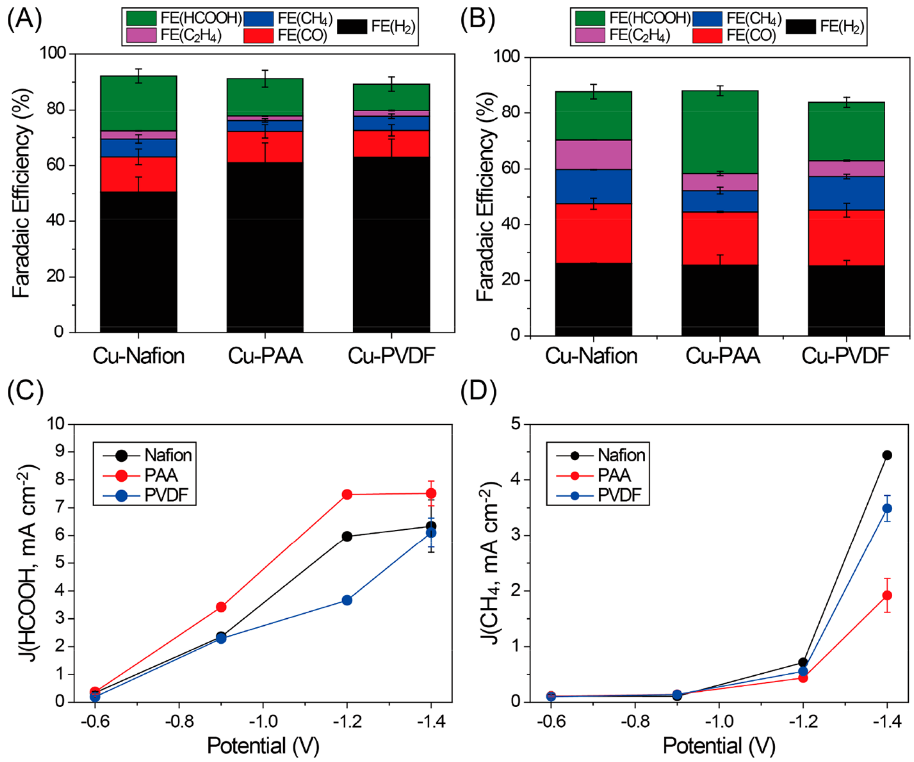

Figure 1. CO_2RR performance of a series of Cu/C catalysts with different binders: (A) FE of HCOOH, CO, CH_4, C_2H_4, and H_2 at −0.6 V; (B) the same consideration at −1.4 V. Partial current density profiles of (C) HCOOH and (D) CH_4.

product distribution originating from modified metal−adsorbate interactions. Furthermore, it has been recently found that the partial pressure of CO_2 can adjust product distribution of CO_2RR over Cu-based catalysts because it can optimize the interactions between different reaction intermediates such as *CO_2, *CO, and *H, *etc.* in an electrolyzer at a practical scale.[26,27]

In the current study, we demonstrate that the electrocatalytic CO_2RR performance of carbon-supported Cu catalysts (Cu/C) can be influenced by the key functional groups of polymeric binders, which are an essential component for electrode fabrication. We adopted hydrophilic and hydrophobic binders with a similar chemical structure (poly(acrylic acid) (PAA, −COOH group) and polyvinylidene difluoride (PVDF, $-CF_2$ group)) to evaluate the effect of the functional groups on the product distribution of the CO_2RR over Cu/C. It was found that HCOOH was the main product (Faradaic efficiency (FE) ≈ 30%) at a potential of −1.4 V versus a reversible hydrogen electrode (V_{RHE}) when the hydrophilic PAA was adopted. In contrast, when the hydrophobic PVDF was used, CH_4 were favorably produced. Such a distinct dependence on the choice of polymeric binders primarily originates from their interactions with intermediates involved in both CO_2RR and HER. Density functional theory (DFT) calculated free energy profiles for the formation of major products (H_2, CO, HCOOH, and CH_4) reveal that the interaction of functional groups with the Cu surface plays an important role in modulating the product distribution of CO_2RR. The findings in this work suggest that a simple binder replacement can be a viable option in tuning the selectivity and activity of Cu-based electrocatalysts for CO_2RR.

2. EXPERIMENTAL AND THEORETICAL METHODS

2.1. Electrochemical Measurements

All of the chemicals in this work were purchased from Sigma-Aldrich unless otherwise noted. All reagents were used without purification. Saturated calomel electrode (SCE) and graphite rod were used as the reference and counter electrodes, respectively. Each Cu/C electrode with a different binder was referred to as Cu−X, with X being the binder (*i.e.*, Cu−Nafion, Cu−PAA, and Cu−PVDF). In the process of fabricating working electrodes, a binder content of 0.5 wt % was selected. The CO_2-saturated 0.1 M potassium bicarbonate ($KHCO_3$) aqueous solution was utilized as an electrolyte. The reference electrode was calibrated using a reversible hydrogen electrode (HydroFlex, ET-070, EDAQ). For CO_2 electrolysis, a typical H-type cell consisting of two airtight compartments was used. The cathodic and anodic compartments were separated by a Nafion 117 membrane. The applied potential was controlled by *i*R-compensation (80%) and converted to the reversible hydrogen electrode (RHE). Here and afterward, all of the potentials (V) are with respect to an RHE potential unless otherwise noticed. See the Supporting Information for the detailed experimental conditions.

The CO_2RR performance was evaluated using the chronoamperometry (CA) method at each constant potential. The gaseous and liquid products were quantified by using gas chromatography (GC, Agilent, Agilent 7890B) and high-performance liquid chromatography (HPLC, Agilent, 1260 Infinity II equipped with Hi-Plex H columns), respectively. The calculations of FE and partial current density (*J*) were the same as described in our previous work.[17,34−37] The detailed procedure is provided in the Supporting Information.

2.2. *In Situ* X-ray Absorption Fine Structure (XAFS)

In situ XAFS measurements were conducted on the 1D beamline (KIST-PAL) at Pohang Light Sources (PLS) in Pohang Accelerating Laboratory (PAL) using fluorescent detection. Each potential was held for 12 min during XAFS measurements. The typical duration for a single spectrum was around 3 min, and four spectra were merged to improve the signal-to-noise ratio.

The obtained spectra were processed using the ATHENA and ARTEMIS software in the IFFEFIT package.[38,39] The procedure described by Ravel et al.[39] was followed during data processing. EXAFS analysis was conducted by using the ARTEMIS software. The k^3-weighted EXAFS spectrum ($\chi(k)$) was used to intensify the signal at a high k-regime. The Hanning window was utilized for the Fourier transform operation. All of the EXAFS fittings were done in the R space. The goodness of fit was evaluated based on the reliable factor (R-factor) and reduced chi-square (reduced χ^2). The representative fitted EXAFS spectra for different catalysts at 0, −1.2, and −1.3 V are shown in Figure S9, and the fitting parameters are tabulated in Table S3.

2.3. DFT Calculations

Spin-polarized DFT calculations[40,41] were performed at the generalized gradient approximation (GGA) level[42] using the plane wave Vienna *Ab-Initio* Simulation Package (VASP) code.[43,44] The core electrons were described using the projector augmented wave (PAW) potentials[45] including the vdW correction with the DFT-D3 method of Grimme et al.[46] using PW91 functionals.[47] A kinetic energy cutoff of 400 eV and 3 × 3 × 1 k-point mesh were used in all structure-optimization calculations.

By considering that the main CO_2RR product in this study is CH_4, the thermodynamically most stable low index Cu(111) surface was selected as a DFT model surface.[48] The Cu(111) surface was modeled using a four-layer 3 × 3 surface slab. Cu−Nafion was modeled as a combination of the $-SO_3H$ and $-CF_2$ preadsorbed on Cu(111).[49−51] Following the previous work of binders on Au(111),[37] the COOH-containing binder on Cu (Cu−PAA in experiments) was represented by COOH preadsorbed on Cu(111), and F-containing binder on Cu (Cu−PVDF in experiments) was represented by CF_2 preadsorbed on Cu(111). A vacuum layer of approximately 15 Å thick was added in the slab cell along the direction perpendicular to the surface to minimize the artificial interactions between the surface and its periodic images. Atoms in the bottom two layers were fixed, while all other atoms were allowed to relax during geometry optimization until the Hellmann−Feynman force on each ion was smaller than 0.02 eV/Å. The details on binding energy, activation energy, and Gibbs free energy calculations are described in the Supporting Information.

3. RESULTS AND DISCUSSION

3.1. Characterization and Electrochemical Measurements

The impact of the surface functional groups of binder species on CO_2RR was evaluated using different binders, which were Nafion, PAA, and PVDF. The resulting Cu/C electrodes were referred to as Cu−X with X being the binder, as shown in Figure S1. In the process of fabricating working electrodes, a binder content was selected to be 0.5 wt % because this binder loading exhibited the highest total current density for CO_2RR compared with binder loadings of 0.05 wt and 5 wt % (Figure S2). High-resolution transmission electron microscopy (HR-TEM) analyses confirmed that the commercial Cu/C has an average Cu particle size of ∼50 nm with a well-defined crystalline feature (Figure S3). The electrochemical CO_2RR performance of a series of Cu−X was examined by using the chronoamperometry (CA) method (Figure S4) in a high-purity CO_2-saturated 0.1 M $KHCO_3$ solution.

Parts A and B of Figure 1 display the FE profiles for various products over Cu−Nafion, Cu−PAA, and Cu−PVDF at −0.6 and −1.4 V, respectively. See Table S1 for detailed FE values. Cu−Nafion, the benchmarking electrode in the current study, produced a mixture of various products including H_2, oxygenated C1 species (CO and HCOOH), and hydrocarbons (CH_4 and C_2H_4), consistent with previous reports on Cu nanoparticles.[52,53] At −0.6 V, HER surpassed CO_2RR, as evidenced by higher FE (H_2, 50.5%) over FE (CO, 12.6%) and FE (HCOOH, 19.8%). However, with increasing applied potential, FE of CO_2RR increased as a result of the suppressed HER (*e.g.*, 50.5% at −0.6 V → 26.1% at −1.4 V). Both FE(CO) and FE(HCOOH) increased up to 28.7% and 32.8% at −0.9 V and then gradually dropped down to 21.5% and 17.4% at −1.4 V, respectively. At the same time, FE(CH_4) and FE(C_2H_4) increased up to 12.2 and 10.6% at −1.4 V, respectively, confirming that the reaction pathway for CO_2RR products was greatly influenced by the applied potential.[54−57] By considering that hydrocarbon production was favored at the expense of H_2, CO, and HCOOH at negative potentials, it could be speculated that the reaction pathways for CH_4 and C_2H_4 involved the hydrogenation step of either formate (*HCOO) or carbon monoxide (*CO) intermediates.

Upon the replacement of Nafion with PAA or PVDF, Cu-based electrodes exhibited similar products detected in the Cu−Nafion electrode. When the applied potential was increased, CO_2RR was generally enhanced while HER tended to be suppressed. However, their CO_2RR product distribution was significantly modified, indicating that the CO_2RR over the Cu surface was sensitively affected by the key functional groups of binders. For example, at −0.9 V, Cu−PVDF was efficient at producing CO and suppressing H_2 evolution. Cu−PVDF exhibited the peak FE(CO) value of 37.4%, while Cu−Nafion and Cu−PAA showed FE(CO) of ∼29%, which might be also associated with its lowest FE (H_2, 20.1%) of Cu−PVDF at the same potential. The product distribution over Cu−Nafion and Cu−PVDF at −1.2 and −1.4 V became generally similar to exhibiting better CH_4 and C_2H_4 produciton compared to Cu−PAA, which could be understood by the similar key functional group ($-CF_2$) in their binder structure.

It should be noticeable that HCOOH was most selectively produced over Cu−PAA with the FE(HCOOH) value of 37.6% at −1.2 V, which was 1.8 and 1.2 times higher than those of Cu−PVDF (21.1%) and Cu−Nafion (30.9%), respectively. Moreover, the high selectivity toward HCOOH over Cu−PAA was maintained with FE(HCOOH) of 29.8% at −1.4 V, which was 1.4−1.7 times higher compared to Cu−PVDF and Cu−Nafion. By considering the recent reports[58,59] that HER is efficiently accelerated in hydrophilic environments, the high FE(HCOOH) values for Cu−PAA suggested that the protons present on the Cu−PAA surface were utilized as a reactant for HCOOH formation rather than for HER even at high overpotentials. Therefore, at −0.9 V and afterward, the surface H generated due to H_2O dissociation on the hydrophilic Cu−PAA catalyst played an important role in tuning the favored CO_2RR pathway.[56] On the contrary, the selective hydrocarbon production was achieved on Cu−PVDF with its FE(CH_4) being ∼1.6 times higher than that of Cu−PAA at −1.4 V, supporting again that the key functional groups effectively modified the reaction pathways. Such enhanced CH_4 production on Cu−PVDF compared to Cu−PAA suggested that the hydrophobic environment near the electrode promoted hydrocarbon reaction pathway.[28,37,60]

Parts C and D of Figure 1 display the partial current density (J) of HCOOH and CH_4, respectively. The partial density profiles of other products are shown in Figure S5. The different current densities of Cu−X electrodes may originate from the different wettabilities of binders in electrodes as well as their different selectivities toward each product.[61−64] Consistent with the trend of FE values, Cu−PAA achieved higher J(HCOOH) over Cu−Nafion and Cu−PVDF over the entire potential ranges. In contrast, Cu−PVDF showed higher CH_4

https://doi.org/10.1021/jacsau.1c00487
JACS Au 2022, 2, 214−222

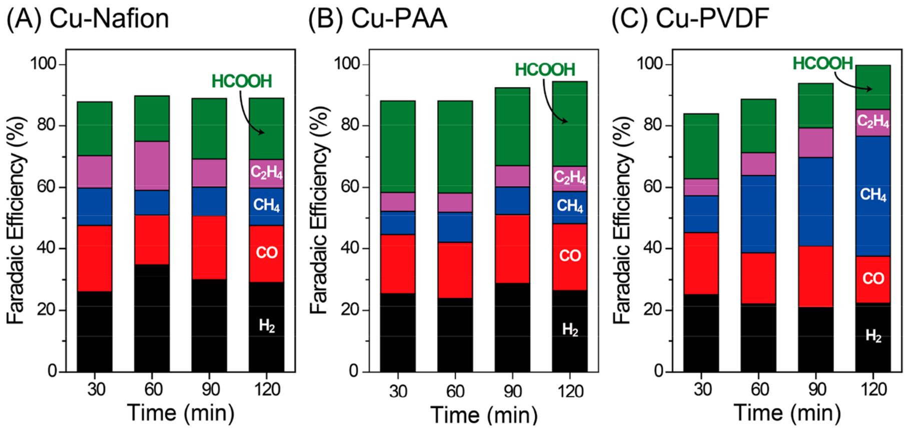

Figure 2. Stability tests at −1.4 V for 2 h. FE profiles of (A) Cu−Nafion, (B) Cu−PAA, and (C) Cu−PVDF.

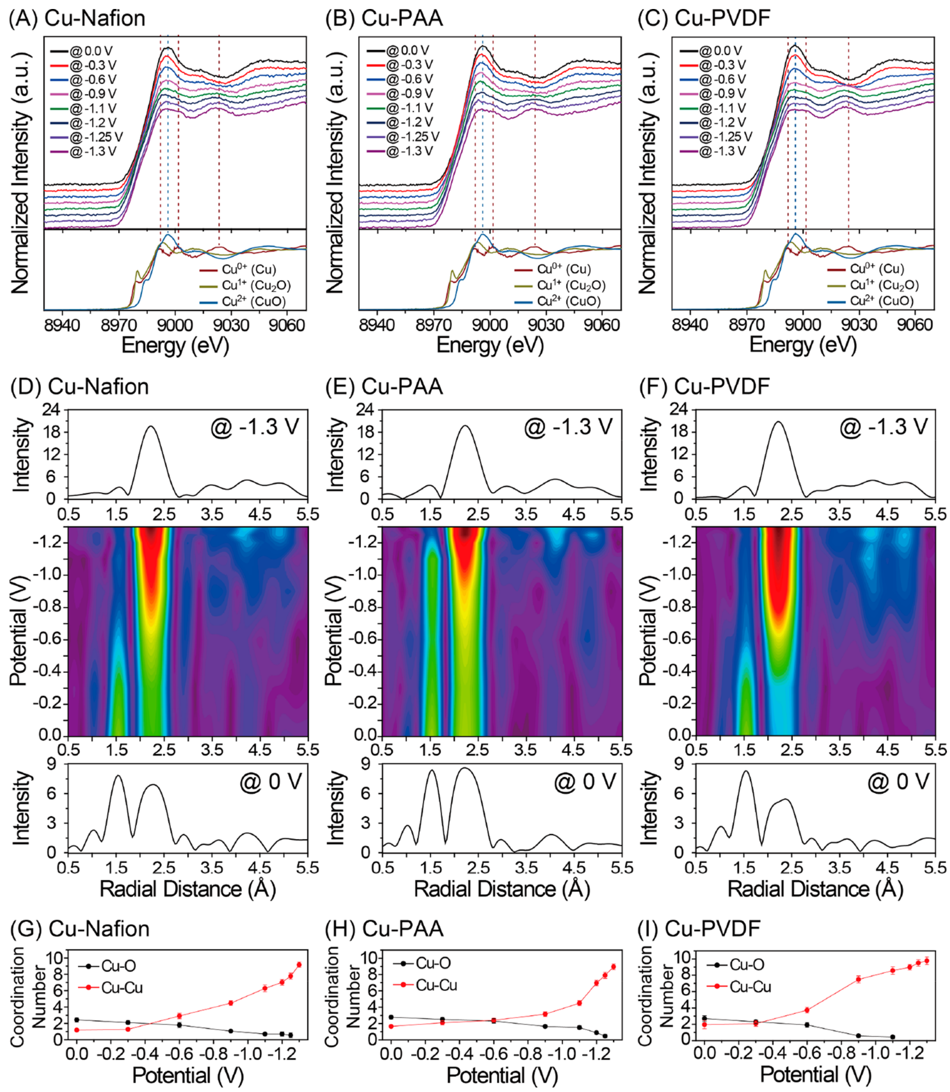

Figure 3. *In situ* XAFS analysis at Cu K-edge. XANES profiles for (A) Cu−Nafion, (B) Cu−PAA, and (C) Cu−PVDF. EXAFS profiles at 0 V (top) and −1.3 V (bottom) and corresponding contour map of EXAFS profiles from 0 to −1.3 V (middle) for (D) Cu−Nafion, (E) Cu−PAA, and (F) Cu−PVDF. Coordination number profiles for Cu−O (Cu_2O, black) and Cu−Cu (Cu, red) for (G) Cu−Nafion, (H) Cu−PAA, and (I) Cu−PVDF.

activity than Cu−PAA at high overpotentials (*e.g.*, 1.9 versus 3.5 mA cm^{-2} at −1.4 V), originating from the surface hydrophobicity of the Cu−PVDF electrode. Overall, Cu−PVDF was more efficient at converting CO_2 to hydrocarbon, while Cu−PAA was better at producing HCOOH throughout all of the potentials in this study.

https://doi.org/10.1021/jacsau.1c00487
JACS Au 2022, 2, 214−222

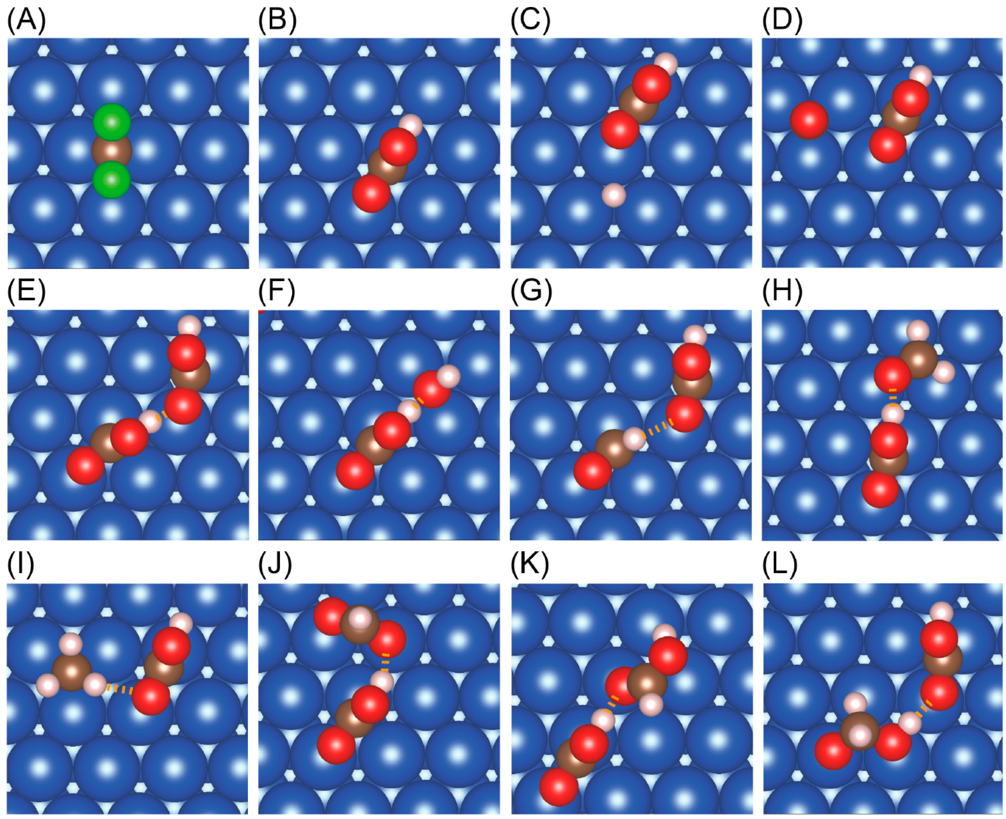

Figure 4. DFT-optimized geometries: (A) CF_2−Cu(111), (B) COOH−Cu(111), and (C–L) *H, *CO, *HOCO, *OH, *HCO, *H_2CO, *H_3CO, *HCOO, *HCOOH, and *H_2COOH on COOH−Cu(111), respectively. Cu: blue, C: brown, F: green, O: red, and H: pink. *X represents species X adsorbed on the surface. Dashed lines in orange represents hydrogen bonding between the adsorbed COOH group and reaction intermediates.

All of the electrodes with different binders maintained their stable electrocatalytic activity for 2 h (Figure 2) at −1.4 V while exhibiting distinguished product distribution depending on the binder. It is interesting that FE(CH_4) of Cu−PVDF increased from 12.0 to 39.0%, supporting again its high selectivity toward CH_4. Thus, this result indicates that Cu−PVDF may require a longer time to reach a steady state. The J profiles of a series of Cu−X electrodes were found to be stable over the same period and exhibited the same trend with their FE profiles (Figure S6). It was also found that their CO_2RR performance was also stable at low potentials such as −0.6 V (Table S2). Cu NPs remained the same after the stability tests regardless of the binder choice as shown in the *ex situ* TEM characterization of spent catalysts (Figure S7). Based on the observation that the electrodes remained firm without being detached from the carbon substrates on the completion of CO_2RR, one can state that the functional groups in each binder would not be degraded (Figure S8).

3.2. *In Situ* XAFS Characterization

To elucidate the active site of Cu/C catalysts modified by different binders, *in situ* XAFS analysis was performed at the Cu K-edge. On the basis of the X-ray absorption near edge structure (XANES) profiles (Figures 3A–C), the commercial Cu/C catalyst used in this study showed a mixed structure of cupric oxide (CuO) and metallic Cu at 0 V. However, with gradual electrochemical reduction reaction from 0 to −1.3 V, regardless of the binder choice, XANES profiles gradually shifted toward lower energy values and the intensity of white lines decreased, indicating that all of the electrodes mainly adopted the feature of metallic Cu as illustrated along the brown dotted lines. Furthermore, the extended-XAFS (EXAFS) profiles in Figure 3D–F reflected the same changes that the initial oxide feature (Cu−O bond at ∼1.5 Å) disappeared with an intensifying metallic Cu bond (Cu−Cu) at ∼2.2 Å. The coordination number profile as a function of applied potential also indicated that, with negatively increasing potentials, the Cu−O bond disappeared while the Cu−Cu bond formed (Figures 3G–I). In addition, the EXAFS fitting results supported the presence of metallic Cu at −1.2 and −1.3 V (Figure S9 and Table S3), suggesting that the metallic Cu surface serves as the catalytic active site for the CO_2RR because all of the electrodes were fully reduced to metallic Cu during the LSV measurement prior to the actual CO_2RR test. Therefore, the different CO_2RR product distributions in this study mainly originated from the modification by the different binders rather than the oxidation state of Cu, allowing one to focus on the effect of the key functional group present in the binders in DFT calculations described below.

3.3. DFT Calculations

DFT calculations[40−47] were performed to gain insight into the role of PAA and PVDF binders on the selectivity of CO_2RR on Cu(111), which represents the energetically most stable low index facet of metallic nanoparticles (∼50 nm) observed in the TEM and scanning TEM (STEM) images (Figures S3 and S7). The DFT calculations were carried out to determine the binding energies of reaction intermediates (Table S4) responsible for the conversion of CO_2 to three C1 products, namely CO, HCOOH, and CH_4. The DFT-calculated models

https://doi.org/10.1021/jacsau.1c00487
JACS Au 2022, 2, 214−222

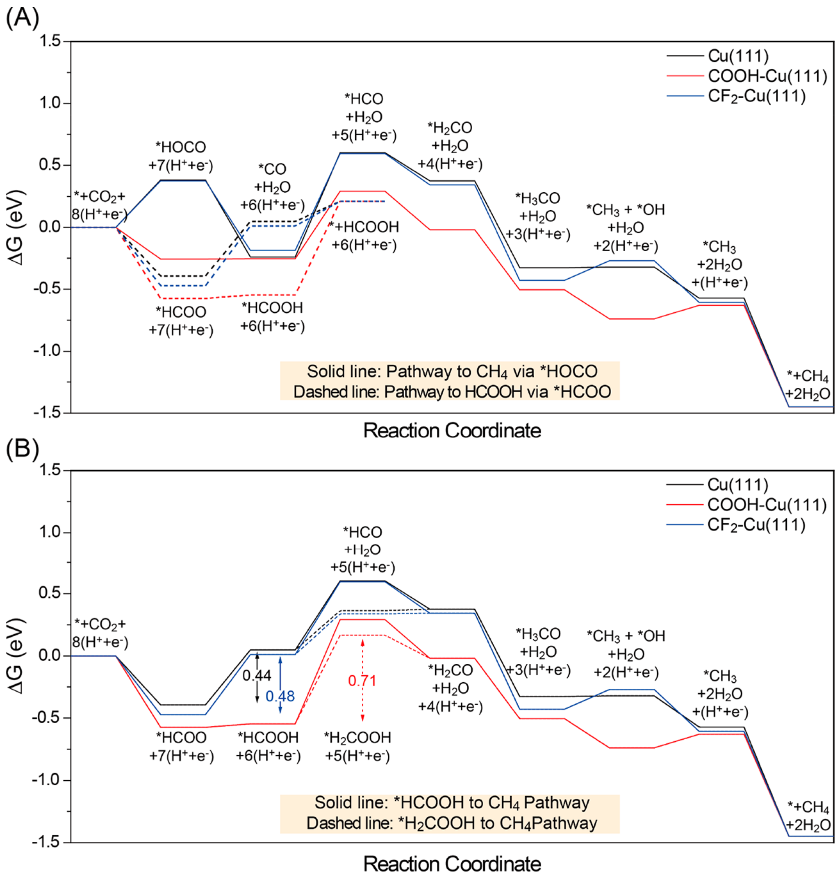

Figure 5. DFT-calculated free energy diagrams of CO_2RR at a potential (U) = 0 V. (A) CO_2 conversion to CO and CH_4 *via* the formation of *HOCO intermediate and to HCOOH *via* the formation of *HCOO intermediate. (B) CO_2 conversion to CH_4 *via* the formation of *HCOO intermediate.

were constructed by reflecting the choice of binders. PVDF and PAA binders were represented by $-CF_2$ and −COOH groups on the Cu(111) surface, respectively, which thus led to $-CF_2$ preadsorbed Cu(111) (CF_2−Cu(111), Figure 4A) and COOH preadsorbed Cu(111) (COOH−Cu(111), Figure 4B). Our focus is to compare the effect of hydrophilic and hydrophobic functional groups. Because Nafion contains both hydrophilic ($-SO_3H$) and hydrophobic ($-CF_2$) groups, DFT of the Nafion/Cu interface does not allow us to conclusively differentiate the role of hydrophilicity on reaction pathways. The comparison with unmodified Cu should provide direct information regarding the effect of hydrophilicity and hydrophobicity on the binding energies of intermediates and the reaction pathways. For comparison, DFT calculations of the reaction network over SO_3H−Cu(111) and CF_2−Cu(111) are overlaid in Figure S10. Experimentally, the CO_2RR activity and selectivity over Cu−Nafion are likely affected by the competing effects of the hydrophilic and hydrophobic groups.

In general, binding sites and configurations of the reaction intermediates were similar on Cu(111), CF_2−Cu(111), and COOH−Cu(111) (Figure 4C−L). However, the reaction intermediates bonded more strongly on COOH−Cu(111) compared to Cu(111) and CF_2−Cu(111), mainly due to hydrogen bonding between the reaction intermediates and the COOH functional group. Hydrogen bonding between intermediates and the CF_2 functional group was not observed in CF_2−Cu(111), most likely due to the hydrophobic nature of the $-CF_2$ group. Such a difference in binding affinity of reaction intermediates should have a profound effect on the CO_2RR selectivity as discussed below.

The DFT-calculated binding energies were used to determine the free energy change (ΔG) for the formation of CO, HCOOH, and CH_4 at a potential (U) = 0 V as shown in Figure 5. Figure 5A shows the formation of CH_4 *via* the intermediate *HOCO and HCOOH *via* the intermediate *HCOO. The first ($H^+ + e^-$) transfer to CO_2 leads to the formation of either *HOCO or *HCOO intermediate. The DFT-calculated results in Figure 5A show that *HCOO formation is energetically favorable over that of *HOCO on Cu(111), CF_2−Cu(111), and COOH−Cu(111). The thermodynamically less favorable formation of *HOCO, a key intermediate for CO_2RR to CO transformation, explains the lower FE(CO) observed in the experiments compared to the FE(HCOOH) at −0.6 V. Further ($H^+ + e^-$) transfer to *HCOO to form *HCOOH, which leaves the catalytic site as the HCOOH product, is uphill on Cu(111) and CF_2−Cu(111). In contrast, this step is nearly thermoneutral on COOH−Cu(111). This suggests that HCOOH is preferentially formed on Cu−PAA at lower applied potential (U), consistent with the experimental observation of higher FE(HCOOH) and J(HCOOH) on Cu−PAA compared to Cu−PVDF (Figure 1). On COOH−Cu(111), the desorption of *HCOOH as a product is associated with the largest ΔG and thus is predicted to be the rate-determining step.

Because the first ($H^+ + e^-$) transfer to CO_2 yields either *HCOO or *HOCO formation and the former is energetically preferred over the latter, the DFT calculation for the CH_4

https://doi.org/10.1021/jacsau.1c00487
JACS Au 2022, 2, 214−222

pathway is focused on the *HCOO intermediate. This consideration is also consistent with the experimental results that, as the potentials negatively increase, FE(HCOOH) and FE(H_2) decrease while FE(CH_4) increases (Figure 1). Figure 5B shows the free energy profile for CO_2 to CH_4 conversion *via* the *HCOO intermediate. Along this route, *HCOO is reduced to *HCOOH. Thus, the formed *HCOOH can undergo ($H^+ + e^-$) transfer to form *H_2COOH or *HCO + H_2O. As shown in Figure 5B, the formation of *H_2COOH (see the dashed lines) is energetically more favorable than the formation of *HCO + H_2O on Cu(111), CF_2−Cu(111), and COOH−Cu(111). Thus, the DFT calculations predict that CO_2 to CH_4 conversion most likely occurs *via* the formation of *H_2COOH intermediate. Additional ($H^+ + e^-$) transfer enables the C−O bond cleavage of *H_2COOH to form *H_2CO + H_2O, with *H_2CO then undergoing ($H^+ + e^-$) transfer reactions to form the final product CH_4. On Cu(111) and CF_2−Cu(111), the step of *HCOO + ($H^+ + e^-$) to *HCOOH has the largest positive change in free energy (∼0.44 and ∼0.48 eV, respectively) among all steps, is predicted to be the potential determining step. The limiting potential (U_L), which is defined as a potential at which all the electrochemical steps along the reaction channel are thermodynamically downhill in energy, for the formation of CH_4 *via* the HCOO intermediate is predicted to be −0.48 V on CF_2−Cu(111). Thus, the formation of CH_4 is expected to be facile at high *U*. On the COOH−Cu(111), the step *HCOOH + ($H^+ + e^-$) to *H_2COOH is predicted to be the potential determining step with a positive free energy change of ∼0.71 eV, and a significantly larger overpotential (compared to CF_2−Cu(111)) is needed for CO_2 to CH_4 transformation on Cu−PAA. The U_L value is determined on COOH−Cu(111) to be −0.71 V, which is significantly higher compared to the values on CF_2−Cu(111). Overall, in agreement with the experimental findings, the DFT results predict that CF_2−Cu(111) is more selective to CH_4 during CO_2RR at high potentials compared to COOH−Cu(111). Consistent with the experimental Faradaic efficiency in Figure 1, the DFT-predicted U_L values for the formation of CH_4 suggest the CH_4 selectivity should be higher on CF_2−Cu(111) than on COOH−Cu(111).

Hydrogen evolution reaction (HER) is a competing reaction in CO_2RR. The DFT-calculated free energy diagrams of HER (Figure S11) show that the HER is favorable at intermediate *U* values on all surfaces considered in the present study. Therefore, H_2 is predicted to be one of the major products of CO_2RR on Cu(111), CF_2−Cu(111), and COOH−Cu(111), consistent with the experimental observation in Figure 1. Overall, the DFT results are consistent with the experimental results and help explain the selectivity differences observed during CO_2RR over different binders attached to the Cu catalysts.

4. CONCLUSIONS

Tuning the product selectivity of CO_2RR on Cu electrodes remains a significant challenge. Here, we demonstrate that the selectivity to HCOOH and CH_4 can be tuned by choosing polymeric binders in the electrode fabrication process. The combined experimental and DFT results show that Cu−PAA (functionalized by a −COOH group) is more selective to HCOOH production compared to Cu−PVDF (functionalized by −CF_2 group) through the entire potential ranges while CH_4 is favorably produced on Cu−PVDF. DFT calculations reveal that different binding energies of reaction intermediates account for the different product distribution on Cu−PAA and Cu−PVDF. Overall, the experimental observations are consistent with the DFT predictions. Results from the current study show that modification of Cu catalysts by key functional groups of polymeric binders, which are required in electrode fabrication, represents a relatively simple and promising methodology to tune the CO_2RR product selectivity. Future studies can include a better understanding of interactions of electrocatalyst surfaces with both carbon chains and various functional groups in polymeric binders, which would further highlight the important role of binders in the CO_2RR performance.

■ ASSOCIATED CONTENT

Supporting Information

The Supporting Information is available free of charge at https://pubs.acs.org/doi/10.1021/jacsau.1c00487.

Methods, electrode pictures, additional electrochemical results, high-resolution TEM images, EXAFS fitting results, and additional DFT results (PDF)

■ AUTHOR INFORMATION

Corresponding Authors

Ah-Hyung Alissa Park − *Department of Chemical Engineering, Department of Earth and Environmental Engineering, and Lenfest Center for Sustainable Energy, The Earth Institute, Columbia University, New York, New York 10027, United States;* orcid.org/0000-0002-6482-3589; Email: ap2622@columbia.edu

Shyam Kattel − *Department of Physics, Florida A&M University, Tallahassee, Florida 32307, United States;* Email: shyam.kattel@famu.edu

Jingguang G. Chen − *Department of Chemical Engineering and Lenfest Center for Sustainable Energy, The Earth Institute, Columbia University, New York, New York 10027, United States; Chemistry Division, Brookhaven National Laboratory, Upton, New York 11973, United States;* orcid.org/0000-0002-9592-2635; Email: jgchen@columbia.edu

Authors

Qiaowan Chang − *Department of Chemical Engineering, Columbia University, New York, New York 10027, United States*

Ji Hoon Lee − *Department of Chemical Engineering, Columbia University, New York, New York 10027, United States; School of Materials Science and Engineering, Kyungpook National University, Daegu 41566, Republic of Korea;* orcid.org/0000-0002-6459-7120

Yumeng Liu − *Department of Chemical Engineering, Columbia University, New York, New York 10027, United States*

Zhenhua Xie − *Chemistry Division, Brookhaven National Laboratory, Upton, New York 11973, United States*

Sooyeon Hwang − *Center for Functional Nanomaterials, Brookhaven National Laboratory, Upton, New York 11973, United States;* orcid.org/0000-0001-5606-6728

Nebojsa S. Marinkovic − *Department of Chemical Engineering, Columbia University, New York, New York 10027, United States*

Complete contact information is available at:
https://pubs.acs.org/10.1021/jacsau.1c00487

Author Contributions

†Q.C., J.H.L., and Y.L. contributed equally to this work.

Notes

The authors declare no competing financial interest.

ACKNOWLEDGMENTS

This research was supported by the U.S. National Science Foundation AccelNet Program (Grant No. 1927336). This work was also supported by the National Research Foundation of Korea (NRF-2021R1G1A1092280). This research used resources at the 1D beamline (KIST-PAL) of the Pohang Light Sources-II (PLS-II) in the Pohang Accelerating Laboratory (PAL). DFT calculations used resources of the Center for Functional Nanomaterials (CFN), which is a U.S. Department of Energy Office of Science Facility, and the Scientific Data and Computing Center, a component of the BNL Computational Science Initiative, as well as the technical support (electron microscopy), at Brookhaven National Laboratory (Contract No. DE-SC0012704); the Extreme Science and Engineering Discovery Environment (XSEDE) was also utilized, which is supported by the National Science Foundation (Grant No. ACI-1548562). Y.L. (No. 201806010243) acknowledges financial support from the China Scholarship Council.

REFERENCES

(1) Hori, Y. i., Electrochemical CO_2 reduction on metal electrodes. In *Modern Aspects of Electrochemistry*; Springer, 2008; pp 89−189.
(2) Lu, Q.; Jiao, F. Electrochemical CO_2 reduction: Electrocatalyst, reaction mechanism, and process engineering. *Nano Energy* **2016**, *29*, 439−456.
(3) Hori, Y.; Wakebe, H.; Tsukamoto, T.; Koga, O. Electrocatalytic process of CO selectivity in electrochemical reduction of CO_2 at metal electrodes in aqueous media. *Electrochim. Acta* **1994**, *39*, 1833−1839.
(4) Gattrell, M.; Gupta, N.; Co, A. A review of the aqueous electrochemical reduction of CO_2 to hydrocarbons at copper. *J. Electroanal. Chem.* **2006**, *594*, 1−19.
(5) Kuhl, K. P.; Cave, E. R.; Abram, D. N.; Jaramillo, T. F. New insights into the electrochemical reduction of carbon dioxide on metallic copper surfaces. *Energy Environ. Sci.* **2012**, *5*, 7050−7059.
(6) Tackett, B. M.; Lee, J. H.; Chen, J. G. Electrochemical conversion of CO_2 to syngas with palladium-based electrocatalysts. *Acc. Chem. Res.* **2020**, *53*, 1535−1544.
(7) Zhang, L.; Zhao, Z. J.; Gong, J. Nanostructured materials for heterogeneous electrocatalytic CO_2 reduction and their related reaction mechanisms. *Angew. Chem., Int. Ed.* **2017**, *56*, 11326−11353.
(8) Peterson, A. A.; Abild-Pedersen, F.; Studt, F.; Rossmeisl, J.; Nørskov, J. K. How copper catalyzes the electroreduction of carbon dioxide into hydrocarbon fuels. *Energy Environ. Sci.* **2010**, *3*, 1311−1315.
(9) Nie, X.; Esopi, M. R.; Janik, M. J.; Asthagiri, A. Selectivity of CO_2 reduction on copper electrodes: the role of the kinetics of elementary steps. *Angew. Chem.* **2013**, *125*, 2519−2522.
(10) Luo, W.; Nie, X.; Janik, M. J.; Asthagiri, A. Facet dependence of CO_2 reduction paths on Cu electrodes. *ACS Catal.* **2016**, *6*, 219−229.
(11) Hahn, C.; Hatsukade, T.; Kim, Y.-G.; Vailionis, A.; Baricuatro, J. H.; Higgins, D. C.; Nitopi, S. A.; Soriaga, M. P.; Jaramillo, T. F. Engineering Cu surfaces for the electrocatalytic conversion of CO_2: Controlling selectivity toward oxygenates and hydrocarbons. *Proc. Natl. Acad. Sci. U. S. A.* **2017**, *114*, 5918−5923.
(12) Zhou, Y.; Che, F.; Liu, M.; Zou, C.; Liang, Z.; De Luna, P.; Yuan, H.; Li, J.; Wang, Z.; Xie, H. Dopant-induced electron localization drives CO_2 reduction to C2 hydrocarbons. *Nat. Chem.* **2018**, *10*, 974−980.
(13) Feng, X.; Jiang, K.; Fan, S.; Kanan, M. W. Grain-boundary-dependent CO_2 electroreduction activity. *J. Am. Chem. Soc.* **2015**, *137*, 4606−4609.
(14) Song, H.; Im, M.; Song, J. T.; Lim, J.-A.; Kim, B.-S.; Kwon, Y.; Ryu, S.; Oh, J. Effect of mass transfer and kinetics in ordered Cu-mesostructures for electrochemical CO_2 reduction. *Appl. Catal., B* **2018**, *232*, 391−396.
(15) Yang, H.; Wu, Y.; Li, G.; Lin, Q.; Hu, Q.; Zhang, Q.; Liu, J.; He, C. Scalable production of efficient single-atom copper decorated carbon membranes for CO_2 electroreduction to methanol. *J. Am. Chem. Soc.* **2019**, *141*, 12717−12723.
(16) Yin, Z.; Gao, D.; Yao, S.; Zhao, B.; Cai, F.; Lin, L.; Tang, P.; Zhai, P.; Wang, G.; Ma, D. Highly selective palladium-copper bimetallic electrocatalysts for the electrochemical reduction of CO_2 to CO. *Nano Energy* **2016**, *27*, 35−43.
(17) Lee, J. H.; Kattel, S.; Jiang, Z.; Xie, Z.; Yao, S.; Tackett, B. M.; Xu, W.; Marinkovic, N. S.; Chen, J. G. Tuning the activity and selectivity of electroreduction of CO_2 to synthesis gas using bimetallic catalysts. *Nat. Commun.* **2019**, *10*, 3724.
(18) Zhu, W.; Tackett, B. M.; Chen, J. G.; Jiao, F., Bimetallic electrocatalysts for CO_2 reduction. In *Electrocatalysis*; Springer, 2020; p 376.
(19) Kim, D.; Resasco, J.; Yu, Y.; Asiri, A. M.; Yang, P. Synergistic geometric and electronic effects for electrochemical reduction of carbon dioxide using gold−copper bimetallic nanoparticles. *Nat. Commun.* **2014**, *5*, 4948.
(20) Ross, M. B.; Dinh, C. T.; Li, Y.; Kim, D.; De Luna, P.; Sargent, E. H.; Yang, P. Tunable Cu enrichment enables designer syngas electrosynthesis from CO_2. *J. Am. Chem. Soc.* **2017**, *139*, 9359−9363.
(21) Ma, S.; Sadakiyo, M.; Heima, M.; Luo, R.; Haasch, R. T.; Gold, J. I.; Yamauchi, M.; Kenis, P. J. Electroreduction of carbon dioxide to hydrocarbons using bimetallic Cu−Pd catalysts with different mixing patterns. *J. Am. Chem. Soc.* **2017**, *139*, 47−50.
(22) Sa, Y. J.; Lee, C. W.; Lee, S. Y.; Na, J.; Lee, U.; Hwang, Y. J. Catalyst−electrolyte interface chemistry for electrochemical CO_2 reduction. *Chem. Soc. Rev.* **2020**, *49*, 6632−6665.
(23) Varela, A. S.; Ju, W.; Reier, T.; Strasser, P. Tuning the catalytic activity and selectivity of Cu for CO_2 electroreduction in the presence of halides. *ACS Catal.* **2016**, *6*, 2136−2144.
(24) Singh, M. R.; Kwon, Y.; Lum, Y.; Ager, J. W., III; Bell, A. T. Hydrolysis of electrolyte cations enhances the electrochemical reduction of CO_2 over Ag and Cu. *J. Am. Chem. Soc.* **2016**, *138*, 13006−13012.
(25) Resasco, J.; Chen, L.; Clark, E.; Tsai, C.; Hahn, C.; Jaramillo, T. F.; Chan, K.; Bell, A. T. Promoter effects of alkali metal cations during electrocatalytic carbon dioxide reduction. *J. Am. Chem. Soc.* **2017**, *139*, 11277.
(26) Song, H.; Song, J. T.; Kim, B.; Tan, Y. C.; Jihun, O. Activation of C_2H_4 reaction pathways in electrochemical CO_2 reduction under low CO_2 partial pressure. *Appl. Catal., B* **2020**, *272*, 119049.
(27) Tan, Y. C.; Lee, K. B.; Song, H.; Oh, J. Modulating local CO_2 concentration as a general strategy for enhancing C−C coupling in CO_2 electroreduction. *Joule* **2020**, *4*, 1104−1120.
(28) García de Arquer, F. P. G.; Dinh, C.-T.; Ozden, A.; Wicks, J.; McCallum, C.; Kirmani, A. R.; Nam, D.-H.; Gabardo, C.; Seifitokaldani, A.; Wang, X. CO_2 electrolysis to multicarbon products at activities greater than 1 A cm^{-2}. *Science* **2020**, *367*, 661−666.
(29) Dinh, C.-T.; Burdyny, T.; Kibria, M. G.; Seifitokaldani, A.; Gabardo, C. M.; De Arquer, F. P. G.; Kiani, A.; Edwards, J. P.; De Luna, P.; Bushuyev, O. S. CO_2 electroreduction to ethylene via hydroxide-mediated copper catalysis at an abrupt interface. *Science* **2018**, *360*, 783−787.
(30) Yang, F.; Mao, X.; Ma, M.; Jiang, C.; Zhang, P.; Wang, J.; Deng, Q.; Zeng, Z.; Deng, S. Scalable strategy to fabricate single Cu atoms coordinated carbons for efficient electroreduction of CO_2 to CO. *Carbon* **2020**, *168*, 528−535.

(31) Jia, M.; Fan, Q.; Liu, S.; Qiu, J.; Sun, Z. Single-atom catalysis for electrochemical CO_2 reduction. *Curr. Opin. Green Sustain. Chem.* **2019**, *16*, 1−6.
(32) Mun, Y.; Lee, S.; Cho, A.; Kim, S.; Han, J. W.; Lee, J. Cu-Pd alloy nanoparticles as highly selective catalysts for efficient electrochemical reduction of CO_2 to CO. *Appl. Catal., B* **2019**, *246*, 82−88.
(33) Zhang, F.; Co, A. C. Direct evidence of local pH change and the role of alkali cation during CO_2 electroreduction in aqueous media. *Angew. Chem., Int. Ed.* **2020**, *59*, 1674−1681.
(34) He, Q.; Liu, D.; Lee, J. H.; Liu, Y.; Xie, Z.; Hwang, S.; Kattel, S.; Song, L.; Chen, J. G. Electrochemical conversion of CO_2 to syngas with controllable CO/H_2 ratios over Co and Ni single-Atom Catalysts. *Angew. Chem., Int. Ed.* **2020**, *59*, 3033−3037.
(35) Sheng, W.; Kattel, S.; Yao, S.; Yan, B.; Liang, Z.; Hawxhurst, C. J.; Wu, Q.; Chen, J. G. Electrochemical reduction of CO_2 to synthesis gas with controlled CO/H_2 ratios. *Energy Environ. Sci.* **2017**, *10*, 1180−1185.
(36) Wang, J.; Kattel, S.; Hawxhurst, C. J.; Lee, J. H.; Tackett, B. M.; Chang, K.; Rui, N.; Liu, C. J.; Chen, J. G. Enhancing activity and reducing cost for electrochemical reduction of CO_2 by supporting palladium on metal carbides. *Angew. Chem., Int. Ed.* **2019**, *58*, 6271−6275.
(37) Lee, J. H.; Kattel, S.; Xie, Z.; Tackett, B. M.; Wang, J.; Liu, C. J.; Chen, J. G. Understanding the role of functional groups in polymeric binder for electrochemical carbon dioxide reduction on gold nanoparticles. *Adv. Funct. Mater.* **2018**, *28*, 1804762.
(38) Kelly, S.; Hesterberg, D.; Ravel, B. Analysis of soils and minerals using X-ray absorption spectroscopy. *Methods of Soil Analysis Part 5—Mineralogical Methods* **2015**, *5*, 387−463.
(39) Ravel, B.; Newville, M. ATHENA, ARTEMIS, HEPHAESTUS: data analysis for X-ray absorption spectroscopy using IFEFFIT. *J. Synchrotron Radiat.* **2005**, *12*, 537−541.
(40) Hohenberg, P.; Kohn, W. Density functional theory (DFT). *Phys. Rev.* **1964**, *136*, B864.
(41) Kohn, W.; Sham, L. J. Self-consistent equations including exchange and correlation effects. *Phys. Rev.* **1965**, *140*, A1133.
(42) Perdew, J. P.; Burke, K.; Ernzerhof, M. Generalized gradient approximation made simple. *Phys. Rev. Lett.* **1996**, *77*, 3865.
(43) Kresse, G.; Furthmüller, J. Efficiency of ab-initio total energy calculations for metals and semiconductors using a plane-wave basis set. *Comput. Mater. Sci.* **1996**, *6*, 15−50.
(44) Kresse, G.; Hafner, J. Ab initio molecular dynamics for open-shell transition metals. *Phys. Rev. B: Condens. Matter Mater. Phys.* **1993**, *48*, 13115.
(45) Blöchl, P. E. Projector augmented-wave method. *Phys. Rev. B: Condens. Matter Mater. Phys.* **1994**, *50*, 17953.
(46) Grimme, S.; Antony, J.; Ehrlich, S.; Krieg, H. A consistent and accurate ab initio parametrization of density functional dispersion correction (DFT-D) for the 94 elements H-Pu. *J. Chem. Phys.* **2010**, *132*, 154104.
(47) Perdew, J. P.; Wang, Y. Erratum: Accurate and simple analytic representation of the electron-gas correlation energy. *Phys. Rev. B: Condens. Matter Mater. Phys.* **2018**, *98*, 079904.
(48) Bagger, A.; Wen, J.; Varela, A. S.; Strasser, P.; Rossmeisl, J. Electrochemical CO_2 reduction: Classifying Cu facets. *ACS Catal.* **2019**, *9*, 7894−7899.
(49) Shi, W.; Baker, L. A. Imaging heterogeneity and transport of degraded Nafion membranes. *RSC Adv.* **2015**, *5*, 99284−99290.
(50) Li, H.; Pan, C.; Zhao, S.; Liu, P.; Zhu, Y.; Rafailovich, M. H. Enhancing performance of PEM fuel cells: Using the Au nanoplatelet/Nafion interface to enable CO oxidation under ambient conditions. *J. Catal.* **2016**, *339*, 31−37.
(51) Isegawa, K.; Kim, D.; Kondoh, H. Chemical state changes of Nafion in model polymer electrolyte fuel cell under oxygen/hydrogen gas atmosphere observed by S-K XANES spectroscopy. *RSC Adv.* **2018**, *8*, 38204−38209.
(52) Wang, Y.; Chen, Z.; Han, P.; Du, Y.; Gu, Z.; Xu, X.; Zheng, G. Single-atomic Cu with multiple oxygen vacancies on ceria for electrocatalytic CO_2 reduction to CH_4. *ACS Catal.* **2018**, *8*, 7113−7119.
(53) Raciti, D.; Wang, C. Recent advances in CO_2 reduction electrocatalysis on copper. *ACS Energy Lett.* **2018**, *3*, 1545−1556.
(54) Kortlever, R.; Shen, J.; Schouten, K. J. P.; Calle-Vallejo, F.; Koper, M. T. Catalysts and reaction pathways for the electrochemical reduction of carbon dioxide. *J. Phys. Chem. Lett.* **2015**, *6*, 4073−4082.
(55) Hu, X.; Yang, H.; Guo, M.; Gao, M.; Zhang, E.; Tian, H.; Liang, Z.; Liu, X. Synthesis and characterization of (Cu, S) Co-doped SnO_2 for electrocatalytic reduction of CO_2 to formate at low overpotential. *ChemElectroChem* **2018**, *5*, 1330−1335.
(56) Tang, Q.; Lee, Y.; Li, D.-Y.; Choi, W.; Liu, C.; Lee, D.; Jiang, D.-e. Lattice-hydride mechanism in electrocatalytic CO_2 reduction by structurally precise copper-hydride nanoclusters. *J. Am. Chem. Soc.* **2017**, *139*, 9728−9736.
(57) Zhu, W.; Kattel, S.; Jiao, F.; Chen, J. G. Shape-controlled CO_2 electrochemical reduction on nanosized Pd hydride cubes and octahedra. *Adv. Energy Mater.* **2019**, *9*, 1802840.
(58) Meng, C.; Wang, B.; Gao, Z.; Liu, Z.; Zhang, Q.; Zhai, J. Insight into the role of surface wettability in electrocatalytic hydrogen evolution reactions using light-sensitive nanotubular TiO_2 supported Pt electrodes. *Sci. Rep.* **2017**, *7*, 41825.
(59) Yue, X.; Huang, S.; Jin, Y.; Shen, P. K. Nitrogen and fluorine dual-doped porous graphene-nanosheets as efficient metal-free electrocatalysts for hydrogen-evolution in acidic media. *Catal. Sci. Technol.* **2017**, *7*, 2228−2235.
(60) Lee, J. H.; Tackett, B. M.; Xie, Z.; Hwang, S.; Chen, J. G. Isotopic effect on electrochemical CO_2 reduction activity and selectivity in H_2O-and D_2O-based electrolytes over palladium. *Chem. Commun.* **2020**, *56*, 106−108.
(61) Wakerley, D.; Lamaison, S.; Ozanam, F.; Menguy, N.; Mougel, V. Bio-inspired hydrophobicity promotes CO_2 reduction on a Cu surface. *Nat. Mater.* **2019**, *18*, 1222−1227.
(62) Buckley, A. K.; Lee, M.; Cheng, T.; Kazantsev, R. V.; Larson, D. M.; Goddard, W.; Toste, F. D.; Toma, F. M. Electrocatalysis at organic-metal interfaces: identification of structure-reactivity relationships for CO_2 reduction at modified Cu surfaces. *J. Am. Chem. Soc.* **2019**, *141*, 7355−7364.
(63) Liang, H. Q.; Zhao, S.; Hu, X. M.; Ceccato, M.; Daasbjerg, K. Hydrophobic copper interfaces boost electroreduction of carbon dioxide to ethylene in water. *ACS Catal.* **2021**, *11*, 958−966.
(64) Yue, P.; Fu, Q.; Li, J.; Zhang, L.; Xing, L.; Kang, Z.; Liao, Q.; Zhu, X. Triple-phase electrocatalysis for the enhanced CO_2 reduction to HCOOH on a hydrophobic surface. *Chem. Eng. J.* **2021**, *405*, 126975.

https://doi.org/10.1021/jacsau.1c00487
JACS Au 2022, 2, 214−222